2024 IEEE/RSJ International Conference on Intelligent Robots and Systems (IROS)
October 14-18, 2024. Abu Dhabi, UAE

Development of a Low Pressure Pouch Sensor for Force Measurement in Colonoscopy Procedures

Korn Borvorntanajanya[1,2], Jabed F Ahmed[3], Mark Runciman[1,3], Enrico Franco[1,2], Nisha Patel[3] and Ferdinando Rodriguez y Baena[*,1,2]

***Abstract*— This paper presents a novel pneumatic pouch sensor, designed to mount on a colonoscope, that can effectively estimate the contact forces with the environment. The pouch sensor was designed to maximize the sensing range, and it was fabricated using a 2D laser welding technique from our track record. A flow compensation (FC) algorithm was introduced to improve the accuracy of the sensor in the presence of static load. The proposed system can reliably measure external forces up to 9.5 N with high repeatability. The system allows discriminating between different levels of force which are typically associated with increasing patient discomfort in colonoscopy: low (0-4 N), medium (4-6 N), and high (>6 N). This system achieves over 80% accuracy in comparison to the ground truth under steady state conditions ($P \leq 0.05$) and maintains over 68% accuracy in dynamic scenarios.**

I. INTRODUCTION

Colonoscopy is a gold standard diagnostic and therapeutic procedure that involves the insertion of a flexible endoscope into the colon to visualize and assess its lining. During this procedure, precise control and delicate manipulation of the colonoscope are essential to ensure successful navigation through the complex and sensitive structure of the colon. Applying excessive force can result in complications such as tissue trauma, perforation and discomfort for the patient. As such, measurements or estimation of contact forces can help the endoscopist to make the procedure safer and to reduce patient discomfort [1], [2]. In addition, a system that can measure or estimate the contact forces can serve as a training tool, decreasing the learning curve for clinicians [3].

Research has increasingly concentrated on measuring forces directly within the colon. For example, [4] focused on capturing forces within a simulated setting, using a phantom model that mimics the conditions of diagnositc colonoscopy. Among the efforts to measure forces *in vivo*, [5] mounted a load cell on the standard colonoscope allowing force measurements from outside the body. Additionally, [6] employed spring-force measurements in a porcine model, and [7] did a study on arm muscles to estimate the force on the colon during an examination. However, none of these studies have measured in real-time the contact force between colon and endoscope.

To achieve accurate force measurements inside a human body, several sensing principles have been investigated, including magnetic sensors, strain gauges, optical sensors, and pneumatic force sensors [8]. Optical and magnetic sensors [9], [10] are advantageous due to their non-contact working principles. However, they present limitations in sensing range, potentially making them unsuitable for capturing the entire spectrum of forces experienced during colonoscopy. Soft optical-based force sensors for colonoscopy have been developed [11], [12] which offer high precision. Challenges arise in their practical application within the human body, stemming from their electrical nature, and there are concerns over their suitability for single-use applications.

In contrast, pneumatic force sensors, with their wide sensing range and rapid response times, have emerged as a promising avenue for force measurement in colonoscopy procedures [13], [14]. Their inherent mechanical nature makes them ideal for sterile clinical settings, eliminating potential electrical risks and interference. Integrating these sensors into clinical practice could provide force detection and improve patient safety and comfort. Furthermore, pneumatic sensors do not provide a direct measurement of the force but rather an estimate of its magnitude that depends on the geometry of the sensor and on the pressure applied.

This paper introduces a novel pneumatic force sensor developed for force estimation during colonoscopy procedures. The main contributions of this paper include the following points.

- The design of a pneumatic sensing patch that takes into account the requirements of diagnostic colonoscopy.
- A new approach to estimate contact forces that integrates changes in air pressure and flow, and that is ideally suited for low pressure applications.

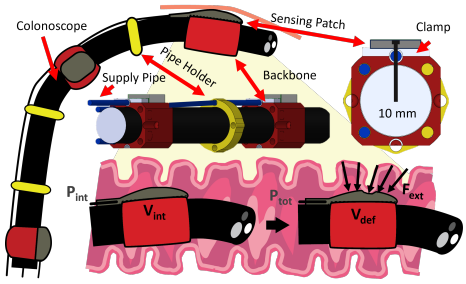

Fig. 1. Schematic overview of the integrated pneumatic sensor system, detailing the key components and the force measurement concept.

*This work was supported by the Engineering and Physical Science Research council (grant no. EP/X033546/1), and by the Multi-scale Medical Robotics Center, The Chinese University of Hong Kong (InnoHK Fund).

[1]The Hamlyn Centre for Robotic Surgery, Imperial College London, United Kingdom.
[2]The Mechatronics in Medicine Laboratory, Imperial College London, United Kingdom.
[3]Department of Surgery & Cancer, Imperial College London, London, United Kingdom
Corresponding author: f.rodriguez]@imperial.ac.uk

II. Methodology

The proposed system integrates multiple sensing patches on a conventional colonoscope. Mounting backbones are employed to affix the sensing patches securely onto the colonoscope and offer a rigid structure that protects them from the tension exerted by the scope. The sensing patches are supplied by pipes, as shown in Figure 1. The pipe holders ensure the correct alignment of the supply pipes for all the sensors integrated onto the scope and minimize pipe deformation. Lastly, the pressure supply, located externally to the human body, provides regulated pressure to the patches, which is used to estimate the forces.

A. Sensing Patch Design

The pneumatic force sensor operates on the principle of converting an applied force into a measurable change in air pressure inside the patch. The sensing patch is composed of sensing pouches, called patterns, that contain pressurized air. When a force is applied to the sensing patch, it deforms the pouches, leading to a corresponding change in pressure. The magnitude of the force can be estimated from the pressure change, see Figure 1.

The maximum volume of the inflated patch (V_{max}) is modelled as in Figure 2. The arc length of the cross section (D_0) is computed as $D_0 = 2r\theta$, with $r\sin(\theta) = \frac{D}{2}$, where r represents the radius of curvature, θ is the angle and D is the length of the chord. The total inflation referred to the initial cross-section of the sensing patch is defined by $\delta(\theta) = \frac{D_0 - D}{D_0} = 1 - \frac{\sin(\theta)}{\theta}$.

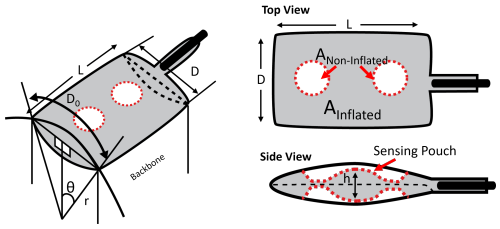

Fig. 2. Dimensions of the pneumatic sensing patch, with areas highlighted in red to indicate the presence of non-inflated areas and sensing pouches.

The theoretical maximum inflation of the sensing patch is calculated by setting θ to $\frac{\pi}{2}$, yielding $\delta(\frac{\pi}{2}) \approx 0.363$ (36%) [15]. The maximum theoretical volume of the sensing patch is computed as

$$V_{max} = \underset{\theta \in (0, \frac{\pi}{2})}{\arg\max}\, V(\theta) = \frac{D_0^2 L}{2}\left(\frac{\theta - \cos(\theta)\sin(\theta)}{\theta^2}\right). \quad (1)$$

The force exerted by the compressed air is determined by integrating the initial pressure over the contact area of the sensing patch. The maximum mechanical work (W_{max}) that the system can undergo through the sensing patch is computed by employing the conservation of energy

$$W_{max} = \int_0^V (P_{int}) dV, \quad (2)$$

where V is the total volume of the sensing patch from (1), (P_{int}) is the initial pressure. The maximum theoretical force (F_{max}) perpendicular to the mid-plane of the sensing patch is

$$F_{max} = \frac{W_{max}}{h} \quad (3)$$

where h is the inflated height of patch. The patches are designed to withstand a maximum force of 10N [7] and are sized to fit a standard colonoscope with a 16.5 mm diameter. From the selected pressure range of 0.25 bar to 0.4 bar (see Section III.A), the dimensions of the patch are determined to be 28.5 mm by 10 mm (L x D), as calculated using equation (3). With these dimensions, the maximum inflated height (h) is calculated to be 3.44 mm based on the ellipse circumference calculation, using D_0 as the circumference and D as the major axis. The minimum radius of curvature (360°) of the colonoscope is increased from 38 mm to 47 mm, which is acceptable in a normal colonoscopy procedures [16], [17]. The overall diameter of the scope with the backbones increases from 16.5 mm to 20 mm, accounting for the height (h) of the pressurized sensing patch, as depicted in Figure 1.

Small pouch patterns are included in the design to ensure a more uniform height, leading to a distributed force measurement across the sensing patch, as depicted in Figure 2. However, the patterns reduce the volume (V) utilized in (2), which impacts the maximum force capability. The maximum forces and their distribution from different designs based on the percentage of inflated area are determined experimentally, see Section III.A. Four different geometries of the sensing patch have been considered, see Table I.

TABLE I
GEOMETRY OF THE SENSING PATCH

Pattern	A	B	C	D
Inflated Area	100%	91%	72%	63%

B. Dynamical Model

1) Pressure-to-Force Conversion Model (PFC): The pressure (P_{ext}) due to an external force (F_{ext}) is calculated as the difference between the total pressure (P_{tot}) and the initial value (P_{int}) [13], [14]:

$$P_{ext} = P_{tot} - P_{int} \quad (4)$$

Due to the complex geometry resulting from the patches, a nonlinear function $(H_{P_{int}})$ is used to describe the relationship between the external force and (P_{ext}) as in

$$F_{ext} = H_{P_{int}}(P_{ext}) \quad (5)$$

The function $H_{P_{int}}$ is estimated using a fourth-order polynomial regression model based on experimental data with the constant initial pressure, see Section III.A.

2) Flow Compensation Model (FC): The sensing patches are supplied by a digital pressure regulator that maintains the system at a constant pressure (P_0). However, connecting the proportional regulator directly to the sensing patch would automatically adjust the internal pressure when an external force acts on the system. Thus, a spring-loaded non-return valve is introduced between the proportional regulator and the sensing patch. This prevents pressure variations due to external forces from affecting the control loop of the digital regulator. However, the spring in the non-return valve results in a pressure drop, that is $P_{int} = P_0 - k(P_0)$, where k is the spring constant.

Due to the combination of low pressure (<0.3 bar) and length of the pipe (>1 m) connecting the pressure source to the patches, the upstream pressure measured by the pressure sensor (P_{iU}) typically differs from the total pressure in the sensing patch (P_{tot}). To address this, we introduce a flow sensor to detect the flow rate (Q) between the pressure sensor and the sensing patch, thereby estimating P_{tot} using P_{iU}, as shown in Figure3. According to ISO 6358, the flow rate (Q) through an equivalent orifice, characterized by conductance (C), is dependent on the upstream pressure (P_{iU}) and downstream pressure (P_{tot}). Computing P_{tot} as a function of the flow rate (Q) , where the flow is considered positive when entering the sensing patch, yields

$$P_{tot} = \begin{cases} P_{iU}\epsilon \frac{1-\sqrt{1-\left(2-\frac{1}{\epsilon}\right)\left(1+\frac{Q^2}{(CP_{iU})^2}(1-\epsilon)^2\right)}}{2\epsilon-1} & \epsilon < \frac{P_{iU}}{P_{tot}} < 1, Q > 0 \\ \frac{Q}{C} & 0 < \frac{P_{iU}}{P_{tot}} \leq \epsilon, Q > 0 \\ P_{iU} & Q = 0 \\ P_{iU}\left(\epsilon + (1-\epsilon)\sqrt{1-\frac{Q^2}{(CP_{iU})^2}}\right) & -CP_{iU} < Q < 0 \\ P_{iU}\epsilon & Q < -CP_{iU}, \end{cases} \tag{6}$$

where ϵ = 0.528 represents the critical pressure ratio for an ideal gas corresponding to sonic flow [18]. The conductance (C) of a pipe with a diameter (D) and length (L) can be expressed as $C = \frac{0.029D^2}{\sqrt{\frac{L}{D^{1.25}}+510}}$.

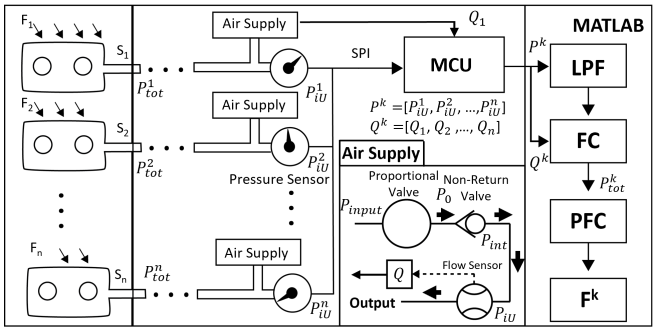

Fig. 3. System schematic showing the integration of multiple sensors with air supply units and their connecting pipelines for force estimation. "LPF" represents the low-pass filter, "FC" denotes the flow compensation model, and "PFC" stands for Pressure-to-Force Conversion.

C. Fabrication Process of Sensing Patch

The sensing patches are produced by welding together two layers of flexible plastic sheet using dimensions as per equation (2) employing a 2-D laser welding machine from our track record [19]. A 0.03 mm thick polyethylene sheet is placed on the vacuum plate of the welding machine. A solvent-based plastic welding material (Clearweld LD940B, Crysta-Lyn, USA) is applied on the plastic sheet using a marker pen, as shown in Figure 4b. Following this step, another layer of plastic sheet is positioned on top of the previous layer with vacuum assistance. The laser then melts and welds the 2 plastic sheets, forming sensing patches with the desired geometry. The sensing patch is then cut and joined to a pipe (i.e., 2 mm diameter and 150 cm in length) using PTFE tape (0.075 mm), and bonded using cyanoacrylate glue, thus ensuring airtight connections. Following these steps, the sensing patches are secured onto the resin-based 3D printed backbones (Veroclear) made with an Objet 260 printer. The backbones are sized to match the dimensions of the sensing patches. A specially designed mechanical clamp ensures airtight connections between the sensing patches and the pipes, reducing air leakage as shown in Figure 4c. This design and fabrication process ensure the integrity and reliability of the pneumatic force sensing system.

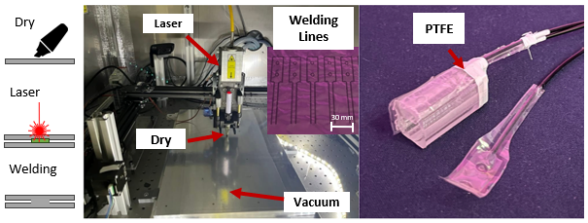

Fig. 4. a) Illustration of the sensing patch fabrication process using laser welding. b) Image of the laser welding machine with the sensing patch placed on the sheets. c) Integration of sensors onto the backbone structure.

D. System Layout

Each sensing patch is connected to the air supply, which includes a proportional pressure regulator (Tecno Basic, Hoerbiger) and a spring-loaded non-return valve (Festo H Series 4mm In/Out). This arrangement permits the regulator to exclusively function as an adjustable pressure supply, as shown Figure 3. Each air supply unit is integrated with a flow sensor (SENSIRION SFM4300-20-P) to detect the direction of air flow (Q) in the system. A digital 14-bit pressure sensor (Te Connectivity 4525DO) converts pressure measurements into digital signals (P^n_{iU}), which are then transmitted to a micro-controller (Arduino Rev4) through an SPI protocol. The micro-controller aggregates sensing data from all the connected sensors and dispatches the combined data (P^k, Q^k) at time k to a computer via serial link with 100 Hz sampling rate and baud rate of 115,200. A low pass filter (LPF) with a 5Hz cut-off frequency (lower than the response time of the digital pressure regulator, which is 100Hz) is then applied to each set of pressure data (P^k). The pressure of the sensing patch (P^k_{tot}) is estimated using (P^k, Q^k) with (6). Subsequently, the pressure data is converted into force values (F^k) using (5).

III. Experimental Results

Two experimental setups have been developed to characterize the proposed sensing system and to assess its performance. The first setup has been employed to identify the design parameters and the design of the sensing patches, to determine suitable values of P_{int}, and to identify F_{max}, and$H_{P_{int}}$. The second setup has been developed to validate the accuracy of the force sensing system integrated with a colonoscope.

A. System Characterization

A robotic arm (KUKA LBR IIWA 7 800) was employed to position a load cell (FSG15N1A) against the sensing patch, applying a force via a contact plate, as illustrated in Figure 5. The end effector moved in 0.15 mm increments along the z-axis, for a total of 4.05 mm from the initial position where a change in P_{tot} was observed. Data was collected across 20 iterations at each step using a 14-bit ADC (Arduino R4 Minima). The external forces ranged from 0 to 16N from the load cell applied as the ground truth of F_{ext}. The maximum force (F_{max}) was determined by the slope $(\Delta F_{ext}/\Delta P_{ext}) \leq 0.002$ bar/N. This indicates a state of complete compression within the sensing patch, where no further change in P_{ext} is observed despite the application of additional external force. The external pressure P_{ext} is calculated from (4) and ΔF_{ext} from a ground truth value set to 0.1 N. This setup was employed for the following three experiments.

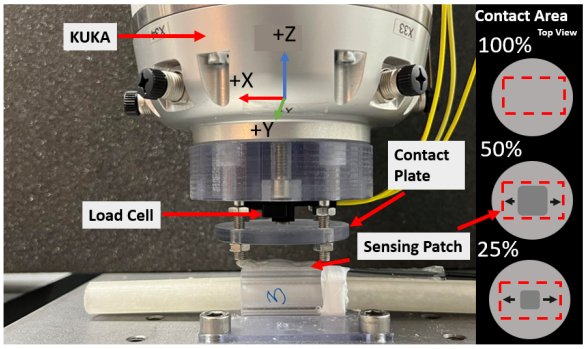

Fig. 5. Characterization experiment comparing the PFC between a load cell and the sensing patch using a robot arm. The experiment features a modified load cell holder and different contact plates.

1) Sensing range and percentage of inflated area: This setup aimed to select the initial pressure (P_{int}) at which the maximum detectable force (F_{max}) is proportional to an increase in pressure. This proportionality occurs when the volume is completely filled by compressed air reaching its maximum value, as defined in (2). The A pattern was employed while the initial pressure was increased from 0.1 bar to 0.5 bar in increments of 0.05 bar. The theoretical maximum force was calculated from (3) and compared with the F_{max}.

The experimental findings indicate that the sensing patch can be safely pressurized up to 0.45 bar, which corresponds to a maximum detectable force of 18 N. Exceeding this threshold can result in irreversible damage to the system leading to air leak. Furthermore, the relationship between the increase in P_{int} and force detection becomes notably linear after P_{int} surpasses 0.25 bar. This marks the system's transition to the maximum volume phase (V_{max}) as shown in Figure 6. Consequentially, P_{int} is selected as 0.3 bar.

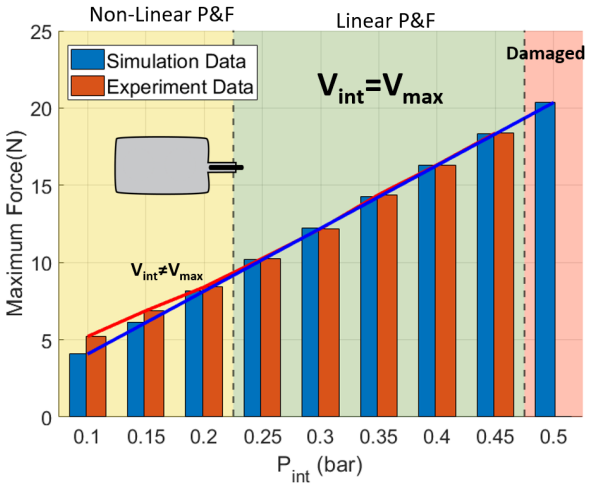

Fig. 6. The relationship between F_{max} and P_{int}, as derived from both calculation and experiments. A linear increase in the initial pressure causes the sensing patches to attain their maximum volume. (Note: the maximum pressure is set at 0.5 bar, and the height (h) in (3) is set to 3.4 mm).

The subsequent set of experiments aimed to determine the most effective design of the sensing pattern among those in Table I. The initial pressure (P_{int}) was set as 0.3 bar, and the maximum force was measured for each design. The experiment was repeated ten times. The percentage of inflated area of the sensing patch was observed to significantly impact the system's sensing ability and its maximum pressure. We found that a larger non-inflated area reduced the detectable F_{max} from 12.1 N to 11.1 N, 9.6 N, and finally to 7.2 N, as shown in Figure 7. These figures correspond to 92%, 78.5%, and 59.5%, respectively of F_{max} for the A pattern, respectively.

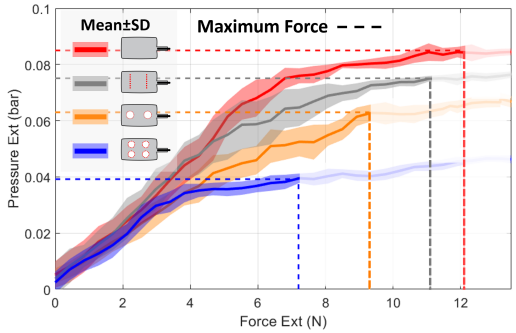

Fig. 7. Relationship between external force/pressure characterization and the pattern design of the sensing patches.The dotted line represents the maximum force measurable at $(P_{int} = 0.3bar)$.

This is expected since a reduction in inflated area corresponds to a reduction in the maximum volume, and consequently in the detectable force. The force distribution was assessed by examining the Pearson correlation coefficient (r)

between P_{ext} and F_{ext}. The calculation of this coefficient from the experimental data yielded values of r = 0.9633, 0.9592, 0.9901, and 0.9566. These values, nearing 1.00, suggest a more linear relationship, which means a more uniform height (h) across the sensing patch. This analysis, coupled with the determination of F_{max}, led to the selection of the C design for subsequent experimentation.

2) Effect of the contact area: Modifications were made to the contact plate, considering three different contact areas: 100%, 50%, and 25%, as depicted in Figure 5. Based on outcomes from prior experiments, the C pattern was chosen for further testing. The robotic arm was programmed to apply forces at these different contact areas while moving along the X axis on the sensing patch. This approach aimed to assess both the maximum force detectable and the characteristics of force distribution. This procedure was conducted five times for each specified contact area, ensuring a thorough assessment of force distribution characteristics. The results shown in Figure 8 indicate a clear proportional relationship between the contact areas and the maximum estimated force: the maximum force was detected at 100% contact area; 49.47% of the maximum force was detected at 50% contact area; 34.21% of the maximum force was detected at 25% contact area. This trend of reduced force detection with decreasing contact areas was consistent even when the applied force did not reach the maximum threshold. Furthermore, there was no significant difference in force detection across various positions of the contact point.

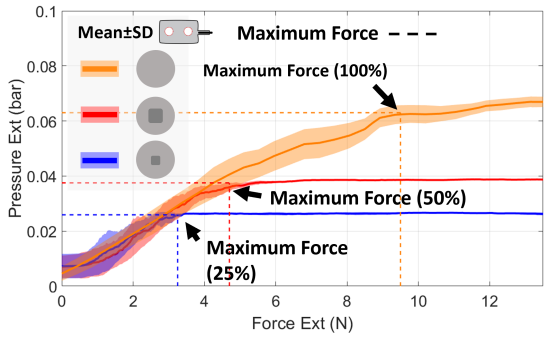

Fig. 8. Relationship between external force/pressure characterization and the contact areas, with the C pattern. (P_{int} = 0.3bar)

3) External force estimation with different sensing patches: The robotic arm applied loads to five different sensing patches, all with the same design (C Design), five times each, to measure the system's repeatability.

The results indicated a variability among sensing patches. These differences arise primarily from the assembly process, particularly the application of adhesive between the sensing patch and the backbone, which may slightly alter the contact area. However, the average standard deviation remained consistent across all sensing patches, with values ranging between a minimum of 0.0016 bar and a maximum of 0.0094 bar, corresponding to 2.5% and 14.9% of sensing range (P_{ext}) respectively. This translates into an error in force estimation from 0.3 N up to 1.8 N. For a further detailed examination, we assessed the average mean and SD values

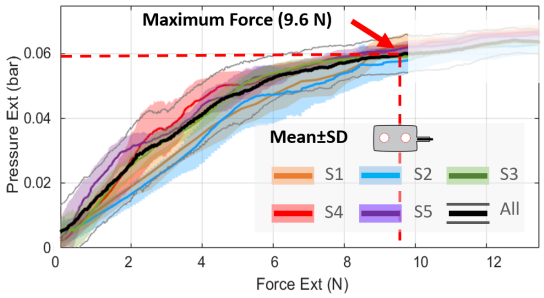

Fig. 9. Relationship between external force/pressure and various sensing patches with the same C pattern design.

for all sensing patches together, as depicted by the black line in Figure 9. The SD value spans from 0.0110 bar to a peak of 0.0277 bar, corresponding to 17.46% and 43.96% of P_{ext} respectively, which potentially diminishes the system accuracy by a factor of 2.95. To address this variability, $H_{P_{int}}$ was modeled separately based on the sensing data obtained from the experiment. Table II provide an example (S1) of a fourth-order polynomial regression applied within the system.

TABLE II

POLYNOMIAL REGRESSION MODEL (5) (P_{int} = 0.3bar)

a_3	a_2	a_1	a_0
1.9 $\times 10^5$	-1.48$\times 10^4$	413.7	-1.937

B. Rigid Phantom Experiment

The sensing patch (S1) was mounted at the tip of the colonoscope, and an initial pressure of 0.3 bar was set, corresponding to the polynomial regression ($H_{P_{int}}$) defined in Table II. To detect the effect of movement-induced deformations on the sensing data, the endoscope was moved in free space without an external payload. F_{ext} was calculated as shown in Figure 10. The maximum RMS error observed while maneuvering the colonoscope in free space (i.e., no-load conditions) was approximately $\pm$0.0219 N.

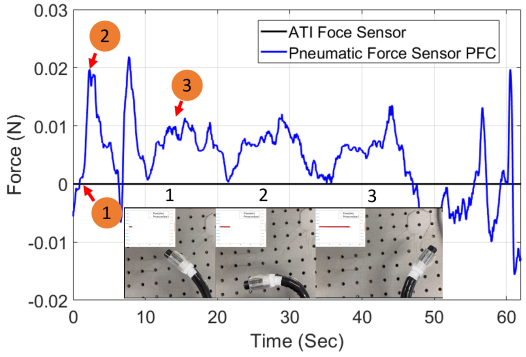

Fig. 10. Free space experiment without load, the changes in force calculation are marked by the numbers 1, 2, and 3, with corresponding colonoscope positions.

A further experiment was conducted by inserting the colonoscope into the rigid phantom shown in Figure 12. During the experiment, the scope touched the rigid phantom

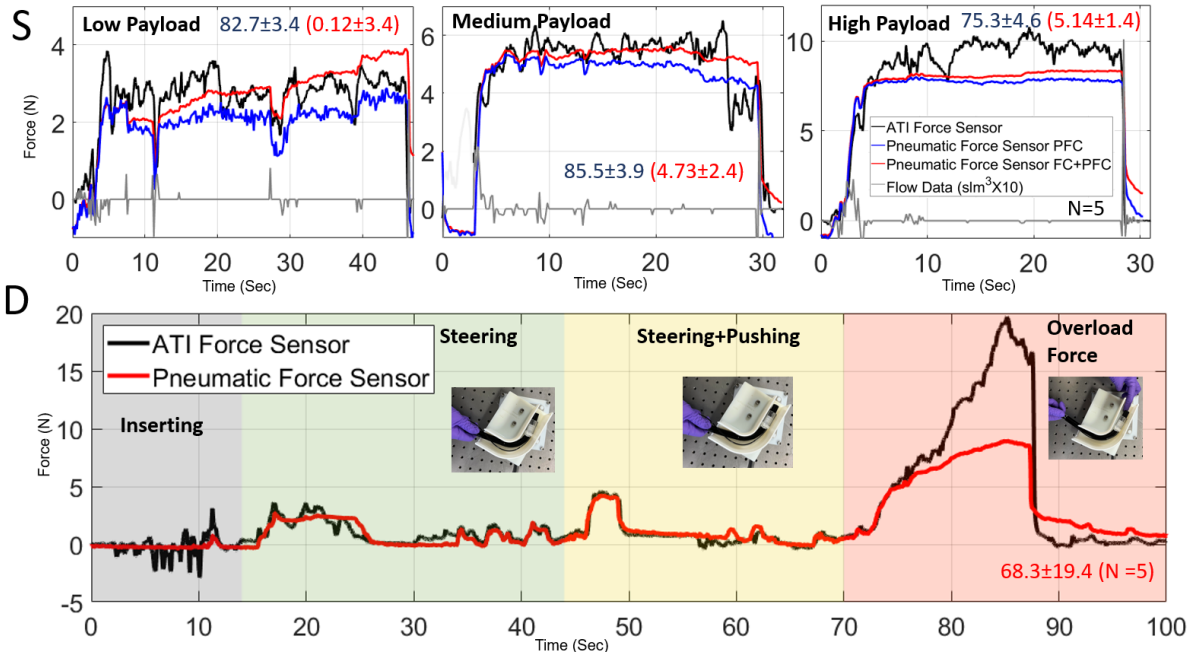

Fig. 11. Multi-directional force measurement, encompassing both PFC and PFC+FC, under static loads across three distinct levels (top) and dynamic loads spanning three different levels (bottom).

only around the sensing patch. The rigid colon phantom, designed in an L shape with a 90-degree bend, was affixed on a Force/Torque sensor (Gamma ATI). The amplitude of the force was calculated by computing the root mean square of the forces along the x and y axes as in $F_{F/T} = \sqrt{F_x^2 + F_y^2}$.

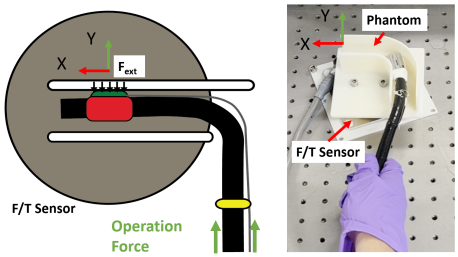

Fig. 12. Experimental setup for multi-directional force measurement. A 90-degree L-shaped phantom is mounted on top of the F/T sensor.

During the experiment, the colonoscope was pushed against the rigid phantom to generate three distinct force levels: low (<0-4N), medium (4-6N), and high (> 6N) [7] corresponding to the average force exerted during colonoscopies. These three levels were generated as follows: the low force level was reached by either steering or pushing, while the medium level was generated by combining the two forces. The high level was achieved when pushing the scope with both hands as shown in Figure 11. During static testing, each of these force levels was maintained for over 20 seconds. For the dynamic test, the force levels were sustained over randomized duration. This process was repeated five times under identical settings by an experienced colonoscopist. The pressure data was then converted into estimated force and compared with ground truth values from the F/T sensor using the Euclidean norm

$$\%similarity = 100 - \frac{100}{I}\sqrt{\sum_{i=1}^{I}\left(\frac{F_{F/T}^i - F_{ext}^i}{F_{F/T}^i}\right)^2},$$

where I represents the number of samples in the experiment when the load was applied to the system. Results indicate that using only the PFC yields similarities of 82.7±3.4%, and, 85.5±3.9%, and 75.3±4.6% compared to the ground truth data for low, medium, and high payloads, respectively. Consequently, the introduction of FC as in (6) can increase the similarity by 0.12±3.4%, 4.73±2.4% and 5.14±1.4%, as shown in Figure 11. This confirms that computing P_{tot} from flow rate helps to compensate the pressure drop due to leakage from the sensing patch. In the dynamic load test, the results show that the system can maintain high accuracy over time across varying payloads, with an overall similarity of 68.3±19.4%.

IV. Discussion & Conclusion

The experimental results indicate that the proposed sensor can estimate contact forces up to 18 N with the A pattern. The initial volume of the air chamber (V_{int}) varies depending on the design of the sensing patch and is influenced by the initial pressure (P_{int}), expressed as (2). Initial experiments indicated that a pressure over 0.25 bar is sufficient to fully inflate the sensing patch as shown in Figure 6. This conclusion was based on the linear relationship observed between the increase in pressure and the maximum detectable force.

The specification of the proposed sensor using the individual regression model is listed in Table III and compared to non-electrical behavior approaches. Importantly, the design of the pattern is crucial in uniformly distributing the force across the patch, resulting in a consistent and linear relationship between F_{ext} and P_{ext}.The subsequent experiments illustrated the effect of the payload's contact area on the sensitivity. Employing the C pattern, changes in the contact area resulted in nearly proportional shifts in the maximum detectable pressure.

TABLE III
SPECIFICATION OF THE SENSING PATCH (C PATTERN) AND COMPARISON

Principle	DxL	F_{max}	RMSE
Fluid*	10x28.5mm	9.6 N	$\pm$ 0.34 N
Optic [11]	62×118 mm	3 N	$\pm$ 0.23 N
Fluid [14]	4.9x3.6 mm	1N	$\pm$ 0.07 N

*This work .

Despite our meticulous patch fabrication process, there are still potential inconsistencies that might emerge during the assembly process. However, this variability is significantly lower than that of silicone pouches (< 3 times), as reported in [14]. The results indicate that, the system can be used to effectively estimate the forces by employing polynomial regression over multiple sensors for the high range of contact forces (>6N). For lower and intermediate force levels, individual calibration remains crucial to ensure optimal accuracy.

Mounting the sensor onto the backbone prevents the stiffness of the scope from influencing the sensing data (RMSE $<$ 0.2281%). In the rigid phantom testing, the pneumatic force-sensing system with individual regression model yields high accuracy (greater than 80 %) for the low and mid force levels ($\leq$6N), which are the most common forces applied during an examination [7]. However, at over maximum force levels (>8N), the small volume of the sensing patch limits the maximum detectable force, resulting in lower resolution ($>$ 70%). Additionally, incorporating the FC feature enhances the system's precision, yielding an improvement of approximately 3%, especially in cases of medium and high payloads. However, the sensor only assesses force magnitude, omitting information such as force/torque direction, which is sufficient for discerning the contact force between a scope and tissues.

Our future research involves assessing these sensors with phantoms representative of human tissue. By integrating a greater number of sensors, we expect to achieve a more comprehensive force profile during endoscopic procedures. Furthermore, enhancements in the assembly process for mounting the sensors are anticipated. These improvements are expected to minimize the maximum RMSE associated with individual sensors and reduce variability between sensors, thereby enhancing the accuracy and reliability of force measurements during clinical applications.

ACKNOWLEDGMENT

The authors are grateful to Pentax Medical for supplying the colonoscope used in this study.

REFERENCES

[1] A. Loeve, P. Breedveld, and J. Dankelman, "Scopes too flexible and too stiff," *IEEE Pulse*, vol. 1, pp. 26–41, 11 2010.
[2] I. Levy and I. M. Gralnek, "Complications of diagnostic colonoscopy, upper endoscopy, and enteroscopy," 10 2016.
[3] D. A. Elphick, M. T. Donnelly, K. S. Smith, and S. A. Riley, "Factors associated with abdominal discomfort during colonoscopy: A prospective analysis," *European Journal of Gastroenterology and Hepatology*, vol. 21, pp. 1076–1082, 9 2009.
[4] A. M. Plooy, A. Hill, M. S. Horswill, A. S. G. Cresp, M. O. Watson, S. Y. Ooi, S. Riek, G. M. Wallis, R. Burgess-Limerick, and D. G. Hewett, "Construct validation of a physical model colonoscopy simulator," *Gastrointestinal Endoscopy*, vol. 76, pp. 144–150, 7 2012.
[5] L. Y. Korman, V. Egorov, S. Tsuryupa, B. Corbin, M. Anderson, N. Sarvazyan, and A. Sarvazyan, "Characterization of forces applied by endoscopists during colonoscopy by using a wireless colonoscopy force monitor," *Gastrointestinal Endoscopy*, vol. 71, pp. 327–334, 2 2010.
[6] M. F. Traeger, D. B. Roppenecker, J. Coy, A. Fiolka, D. Wilhelm, A. Schneider, Meining, Alexander, H. Feussner, T. C. Lueth, and Institute of Electrical and Electronics Engineers, "Forces in minimally invasive surgery: Reliable manipulation of gastric mucosa and the sigmoid colon," 2014.
[7] A. K. Shergill, K. R. Asundi, A. Barr, J. N. Shah, J. C. Ryan, K. R. McQuaid, and D. Rempel, "Pinch force and forearm-muscle load during routine colonoscopy: a pilot study," *Gastrointestinal Endoscopy*, vol. 69, pp. 142–146, 1 2009.
[8] H. Gao, X. Ai, Z. Sun, W. Chen, and A. Gao, "Progress in Force-Sensing Techniques for Surgical Robots," *Journal of Shanghai Jiaotong University (Science)*, vol. 28, pp. 370–381, 6 2023.
[9] M. Lambeta, P. W. Chou, S. Tian, B. Yang, B. Maloon, V. R. Most, D. Stroud, R. Santos, A. Byagowi, G. Kammerer, D. Jayaraman, and R. Calandra, "DIGIT: A Novel Design for a Low-Cost Compact High-Resolution Tactile Sensor with Application to In-Hand Manipulation," *IEEE Robotics and Automation Letters*, vol. 5, pp. 3838–3845, 7 2020.
[10] T. P. Tomo, M. Regoli, A. Schmitz, L. Natale, H. Kristanto, S. Somlor, L. Jamone, G. Metta, and S. Sugano, "A New Silicone Structure for uSkin - A Soft, Distributed, Digital 3-Axis Skin Sensor and Its Integration on the Humanoid Robot iCub," *IEEE Robotics and Automation Letters*, vol. 3, pp. 2584–2591, 7 2018.
[11] M. McCandless, A. Gerald, A. Carroll, H. Aihara, and S. Russo, "A Soft Robotic Sleeve for Safer Colonoscopy Procedures," *IEEE Robotics and Automation Letters*, vol. 6, pp. 5292–5299, 7 2021.
[12] A. Gerald, R. Batliwala, J. Ye, P. Hsu, H. Aihara, and S. Russo, "A Soft Robotic Haptic Feedback Glove for Colonoscopy Procedures," in *IEEE International Conference on Intelligent Robots and Systems*, vol. 2022-October, pp. 583–590, Institute of Electrical and Electronics Engineers Inc., 2022.
[13] M. R. Mitchell, C. McFarland, and M. M. Coad, "Soft Air Pocket Force Sensors for Large Scale Flexible Robots," in *2023 IEEE International Conference on Soft Robotics, RoboSoft 2023*, Institute of Electrical and Electronics Engineers Inc., 2023.
[14] L. Lindenroth, J. Merlin, S. Bano, J. G. Manjaly, N. Mehta, and D. Stoyanov, "Intrinsic Force Sensing for Motion Estimation in a Parallel, Fluidic Soft Robot for Endoluminal Interventions," *IEEE Robotics and Automation Letters*, vol. 7, pp. 10581–10588, 10 2022.
[15] R. Niiyama, X. Sun, C. Sung, B. An, D. Rus, and S. Kim, "Pouch motors: Printable soft actuators integrated with computational design," *Soft Robotics*, vol. 2, pp. 59–70, 6 2015.
[16] M. C. Choy, M. Matharoo, and S. Thomas-Gibson, "Diagnostic ileocolonoscopy: Getting the basics right," *Frontline Gastroenterology*, vol. 11, pp. 484–490, 11 2020.
[17] A. Alazmani, A. Hood, D. Jayne, A. Neville, and P. Culmer, "Quantitative assessment of colorectal morphology: Implications for robotic colonoscopy," *Medical Engineering and Physics*, vol. 38, pp. 148–154, 2 2016.
[18] S. Joshi, H. Sonar, and J. Paik, "Flow path optimization for soft pneumatic actuators: Towards optimal performance and portability," *IEEE Robotics and Automation Letters*, vol. 6, pp. 7949–7956, 10 2021.
[19] M. Runciman, J. Avery, M. Zhao, A. Darzi, and G. P. Mylonas, "Deployable, Variable Stiffness, Cable Driven Robot for Minimally Invasive Surgery," *Frontiers in Robotics and AI*, vol. 6, 1 2020.